
Article:
Xu, J., Odavic, M. orcid.org/0000-0002-2104-8893, Zhu, Z.Q. orcid.org/0000-0001-7175-3307 et al. (2 more authors) (2021) Switching-table-based direct torque control of dual three-phase PMSMs with closed-loop current harmonics compensation. IEEE Transactions on Power Electronics, 36 (9). pp. 10645-10659. ISSN 0885-8993

https://doi.org/10.1109/tpel.2021.3059973

Switching-Table-Based Direct Torque Control of Dual Three-Phase PMSMs with Closed-Loop Current Harmonics Compensation

Jin Xu, Milijana Odavic, Zi-Qiang Zhu, *Fellow*, *IEEE*, Zhan-Yuan Wu, and Nuno Freire

***Abstract*—In this paper, the new closed-loop current harmonics compensation strategy is introduced in the switching-table-based direct torque control (ST-DTC) of dual three-phase permanent magnet synchronous machines (dual 3-ph PMSMs). The harmonic current distortion is the major problem of ST-DTC of multiphase machines and is typically caused by the lack of control in the auxiliary x-y subspace under the vector space decomposition model. The synthetic vectors to obtain average zero voltage in the x-y subspace can be a solution. However, this cannot compensate for current harmonics, for example, due to dead-time and back-electromotive force distortion, which are also mapped into the x-y subspace. Therefore, in this work the x-y voltage references are obtained by the closed control loop that controls x-y currents to zero. To modulate the non-zero x-y voltage reference, the new modulation approach employing voltage vector groups in x-y subspace together with the new switching table is developed and incorporated into ST-DTC. Meanwhile, the analysis of the two available sets of twelve voltage vector groups illustrates a trade-off between linear range in x-y subspace and the DC link voltage utilization rate. Finally, the effectiveness of the proposed ST-DTC strategy is verified through experiments and simulation.**

***Index Terms*— Current harmonics, direct torque control, dual three-phase permanent magnet synchronous machines.**

NOMENCLATURE

Ψ_{fd}	Rotor flux.
T_e	Electromagnetic torque.
θ_s	Stator flux angular position.
θ_e	Electrical angular position.
ω	Mechanical angular speed.
H_Ψ, H_T	Control outputs of flux and torque hysteresis controllers.
R_s	Stator winding resistance.
T_s	Sampling period.
V_{DC}	DC link voltage.
$u_A, u_B, u_C, u_U, u_V, u_W$	Machine phase voltages.
$i_A, i_B, i_C, i_U, i_V, i_W$	Machine phase currents.
$u_\alpha, u_\beta; i_\alpha, i_\beta; L_{\alpha e}, L_{\beta e}; \Psi_\alpha, \Psi_\beta$	Voltages, currents, inductances, and flux linkage in α-β subspace.
$u_x, u_y; i_x, i_y; L_x, L_y; \Psi_x, \Psi_y$	Voltages, currents, inductances, and flux linkage in x-y subspace.
P	Number of pole pairs

This work was supported by the UK EPSRC Prosperity Partnership "A New Partnership in Offshore Wind" under Grant No. EP/R004900/1."

Jin Xu, Milijana Odavic and Zi-Qiang Zhu are with Department of Electronic and Electrical Engineering, University of Sheffield, Sheffield, U.K. (e-mail: jxu60@sheffield.ac.uk; m.odavic@sheffield.ac.uk; z.q.zhu@sheffield.ac.uk). Zhan-Yuan Wu is with Sheffield Siemens Gamesa Renewable Energy Research Centre, Sheffield, U.K. (e-mail: Zhan-Yuan.Wu@siemensgamesa.com). Nuno Freire is with Siemens Gamesa Renewable Energy AS, Brande, Denmark. (e-mail: Nuno.Freire@siemensgamesa.com).

I. INTRODUCTION

MULTI-PHASE drives are increasingly used in high-power and high-current applications as the increased number of phases offer enhanced power handling capacities compared to the three-phase drives. Typical applications are ships propulsion, electric/hybrid vehicles and more electric aircraft, where fault-tolerance is the critical concern and the increased number of phases can provide the required degree of redundancy. Direct torque control (DTC) is characterized by fast torque response and simple structure and has been widely employed for three-phase machines [1]-[8]. It is also increasingly adopted for multi-phase machines [9]-[11], where examples include five-phase induction machines [12]-[14], asymmetric six-phase induction machines [15]-[20], and dual three-phase permanent magnet synchronous machines (dual 3-ph PMSMs) [21]-[22].

Some of the common challenges of DTC are high torque ripple and variable switching frequency. Over the years, the research has been undertaken to overcome the drawbacks of the classical ST-DTC for three-phase machines by introducing relatively more precise control of stator flux amplitude and torque [4]-[8]. However, the major concern of ST-DTC for multiphase machines is large unwanted stator current low-order harmonics caused by the uncontrolled voltage in x-y subspace and inherent system harmonics (for example, dead-time and back-electromotive force (back-emf) distortion), which are most dominant in multi-phase drives compared with their three-phase equivalents, as explained in detail below.

The ST-DTC for dual 3-ph machines is based on the decoupled model of dual 3-ph PMSMs applying the vector space decomposition (VSD) technique [19], which can map machine variables in the three two-dimensional orthogonal subspaces, namely, α-β, x-y, and o1-o2. The fundamental component and mth order harmonics with $m = 12n \pm 1$ ($n = 1,2,3 \cdots$) are mapped into the α-β subspace. The mth order harmonics with $m = 6n \pm 1$ ($n = 1,3,5 \cdots$) are mapped into

the x-y subspace. As the machine with isolated neutral points of the two stator sets is considered here, all voltage vectors in the auxiliary o1-o2 subspace are zero and no current harmonics will be generated in this subspace. If the switching table for multiphase drives is designed following the same principles as for the three-phase drives, only one voltage vector is applied during one sampling period. The voltage vector selection is decided considering only inverter vectors mapped into the torque producing α-β subspace. This inevitably leads to uncontrolled voltage vectors in the auxiliary harmonic producing x-y subspace and will excite large x-y currents.

The solution to the current harmonics caused by the uncontrolled voltage in x-y subspace has been addressed in the literature by introducing modified switching tables. In [20], the modified switching table is developed for a two-level six-phase inverter fed dual 3-ph machine, whereby the voltage vector selection takes into account the effects of voltage vectors on the x-y stator flux. The current harmonics excited in the x-y subspace are proportional to the x-y stator flux, therefore, by selecting voltage vectors that will cause a decrease in the x-y stator flux, the x-y currents can be reduced. The same argument underpins the voltage vector selection strategy in [16], in which the modified switching tables for DTC of a six-phase induction machine are developed. In [21] the problem of the uncontrolled voltage in x-y subspace in dual 3-ph PMSM drives with ST-DTC is solved by developing 12 synthetic vectors, where each synthetic vector comprises two inverter voltage vectors. Two voltage vectors are thus employed in one sampling period and the dwell times of these vectors are calculated (offline) in order to achieve zero average x-y voltage. This approach is further extended in [22] by developing two types of synthetic vectors where the selection between them is decided in order to achieve torque ripple reduction (using a multi-level hysteresis torque controller). The simplified methods of synthetic vector implementation using both FPGA and DSP technologies are presented in detail in [17]. Additionally, the synthetic vector theory reducing current harmonics is extended to five-phase [23] and seven-phase [24] voltage source inverter systems, incorporated into the model predictive control.

For the current harmonics caused by, for example, inverter dead-time and back-emf distortion, they are mainly fifth and seventh harmonics [25]-[26], and decoupled into x-y subspace. Harmonic compensation strategies for multi-phase drives employing ST-DTC in terms of this part of current harmonics have not been reported in the literature, but there exist some compensation strategies based on the field-oriented control (FOC) with PWM.

Of note, this type of current harmonics exists in drives of 3-ph machines and therefore the composition methods based on FOC with PWM could be extended to dual 3-ph machines. In [27], the main 5th and 7th order harmonics are firstly detected and then compensated by a model-based feedback voltage injection or a PI controller. Moreover, a zero-axis current regulator can be added in the control loop to suppress current harmonics [28]. Also, a repetitive controller [29] or a resonant controller [30] can be paralleled to the PI controller to suppress current harmonics further.

The effect of inverter dead-time on the stator current harmonic distortion is more significant in multi-phase drives compared with their three-phase counterparts, as demonstrated in [31] for a five-phase induction motor drive where the dominant 3rd harmonic is present in stator currents. Low-order harmonics generated in each inverter leg voltage of a multi-phase drive are mapped into the x-y subspace where impedances presented to these harmonics are very low (comprise only stator resistance and leakage inductance). On the contrary, in three-phase machines, these harmonics are mapped into the α-β subspace where they are exposed to higher impedances. The control strategies to compensate for these unwanted x-y current harmonics have been developed and successfully integrated into FOC with PWM for various multi-phase machines, as in [26], [31]-[33]. For harmonic compensation strategies in FOC for both 3-ph machines and multi-phase machines, the voltage references to compensate current harmonics can be directly modulated into the switching sequence through PWM techniques, then delivered to phase voltages.

However, no such strategies are developed for ST-DTC of multi-phase machines. The main challenge is that there is typically no modulation in ST-DTC for multi-phase drives, due to the reasons that dwell times of voltage vectors and duty cycles are determined by the switching table and no current control loops are involved in ST-DTC. To fill this literature gap, this paper proposes a novel ST-DTC based current harmonic compensation strategy for dual 3-ph PMSMs. This proposed ST-DTC strategy inherits advantages of direct torque control in α-β subspace, but also provides an approach of modulating voltage references in x-y subspace generated from current controllers into the switching sequence, thereby suppressing stator current harmonics, such as those caused by inverter dead-time and back-emf distortion.

The structure of this paper is organized as follows. Section II presents the voltage source inverter (VSI)-fed dual 3-ph PMSM drive structure, the machine model and VSI switching vectors mapped into the two-dimensional α-β and x-y subspaces. The limitations of the classical ST-DTC and the synthetic vector ST-DTC for dual 3-ph PMSMs, are analyzed in Section III. Section IV presents the new closed-loop current harmonics compensation ST-DTC strategy for dual 3-ph PMSMs, followed by the DC link voltage utilization analysis in Section V. The experimental and simulation results are included in Section VI and Section VII, respectively, to demonstrate the effectiveness of the proposed harmonics mitigation strategy.

II. Structure of Drive System and Mathematical Machine Model

The basic structure of a VSI-fed dual 3-ph PMSM drive system is shown in Fig. 1. The machine with isolated neutral points of the two sets, is considered in this work. Assuming sinusoidal winding distribution and neglecting core losses and magnetic saturation, the mathematical model of a dual 3-ph PMSM can be described by (1) - (3).

It is evident from (3) that only components in α-β subspace are involved in torque generation. This is used to simplify

machine control from the six to two-dimensional problem. However, from (1) and (2) it is also clear that even small voltage components in x-y subspace will cause high current harmonics, as x-y impedances could be generally small, determined only by stator resistance and leakage self-inductance. Therefore, although torque can be controlled by considering only α-β subspace, that will not result in good machine performance, as discussed later in Section III.

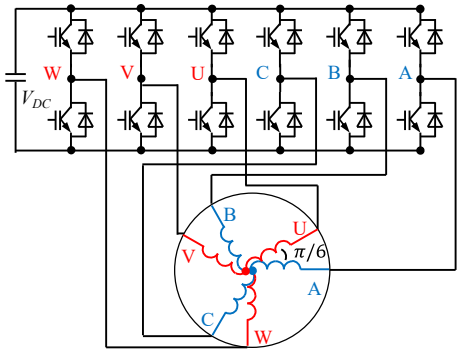

Fig. 1 VSI-fed dual 3-ph PMSM drive structure.

$$\begin{bmatrix} u_\alpha \\ u_\beta \\ u_x \\ u_y \end{bmatrix} = \begin{bmatrix} R_s & 0 & 0 & 0 \\ 0 & R_s & 0 & 0 \\ 0 & 0 & R_s & 0 \\ 0 & 0 & 0 & R_s \end{bmatrix} \begin{bmatrix} i_\alpha \\ i_\beta \\ i_x \\ i_y \end{bmatrix} + \begin{bmatrix} \dot{\Psi}_\alpha \\ \dot{\Psi}_\beta \\ \dot{\Psi}_x \\ \dot{\Psi}_y \end{bmatrix} \tag{1}$$

$$\begin{bmatrix} \Psi_\alpha \\ \Psi_\beta \\ \Psi_x \\ \Psi_y \end{bmatrix} = \begin{bmatrix} L_{\alpha e} & 0 & 0 & 0 \\ 0 & L_{\beta e} & 0 & 0 \\ 0 & 0 & L_x & 0 \\ 0 & 0 & 0 & L_y \end{bmatrix} \begin{bmatrix} i_\alpha \\ i_\beta \\ i_x \\ i_y \end{bmatrix} + \begin{bmatrix} \cos(\theta_e) \\ \sin(\theta_e) \\ 0 \\ 0 \end{bmatrix} \Psi_{fd} \tag{2}$$

$$T_e = 3P(\Psi_\alpha i_\beta - \Psi_\beta i_\alpha) \tag{3}$$

The two-level six-phase VSI, employed in this work, has 64 switching states, where each inverter state can be represented by the corresponding voltage space vector, resulting in a total of 64 available voltage vectors. These vectors can be mapped into the α-β and x-y subspaces as shown in Fig. 2. The vector numbers in Fig. 2 denote the inverter switching states. They are defined as the decimal number values of the six-bit binary numbers formed of ($S_W S_V S_U S_C S_B S_A$), where $S_w, S_V, ..$ denote the switching states of inverter legs $W, V, ..$, respectively, and are either '1' (the upper device is ON) or '0' (the bottom device is ON).

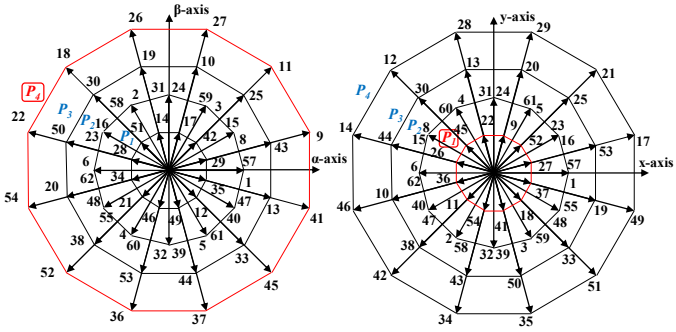

Fig. 2 Voltage vectors of two-level six-phase VSI mapped into α-β and x-y subspaces.

The active voltage vectors can be grouped based on their amplitudes into the four dodecagons, namely P_1, P_2, P_3 and P_4, as shown in Fig. 2, where P_1 denotes the vectors with the smallest amplitude, while P_4 denotes the vectors with the largest amplitude. It can be seen from Fig. 3 that P_4 vectors in α-β subspace fall into dodecagon P_1 in x-y subspace and vice versa. The amplitudes corresponding to the four dodecagons are given by:

$$\begin{cases} L_{P1} = \dfrac{\sqrt{6}-\sqrt{2}}{6} \cdot V_{DC} \\ L_{P2} = \dfrac{1}{3} \cdot V_{DC} \\ L_{P3} = \dfrac{\sqrt{2}}{3} \cdot V_{DC} \\ L_{P4} = \dfrac{\sqrt{6}+\sqrt{2}}{6} \cdot V_{DC} \end{cases} \tag{4}$$

III. Classical ST-DTC and Synthetic Vector ST-DTC

The classical ST-DTC for dual 3-ph PMSMs is obtained by extending the classical ST-DTC for 3-ph PMSMs with small modifications in the switching table. As α-β subspace is relevant for torque generation, the classical ST-DTC for dual 3-ph PMSMs is also implemented in this subspace. In order to maximize the inverter DC link voltage utilization and to assure fast torque response, only vectors from dodecagon P_4 are used. These 12 vectors divide the α-β subspace into 12 sectors, as can be seen in Fig. 3(a). Sectors are selected based on the position of the stator flux linkage vector $\Psi_{\alpha\beta}$, as shown in Fig. 3(b). In general, considering one sampling period, if $\Psi_{\alpha\beta}$ is located in Sector k ($k = \mathrm{I}, \mathrm{II}, .., \mathrm{XII}$), only one vector is selected based on Table I and applied during the whole sampling period. Fig. 3(b) highlights the four possible vectors that can be used if $\Psi_{\alpha\beta}$ is in Sector I, where vectors V_{27} and V_{26} will increase torque, while vectors V_{37} and V_{36} will decrease torque. Vectors V_{27} and V_{37} will result in an increase in the flux amplitude, while vectors V_{26} and V_{36} will results in a decrease in the flux amplitude. One vector is then selected based on the signs of the torque and flux amplitude errors provided by the torque and flux hysteresis controllers, respectively. However, the selected switching states (vectors) will appear as P_1 vectors in x-y subspace which are not controlled and thus x-y current harmonics will be excited. The classical ST-DTC is discussed here to identify the origin of stator current harmonic distortion, however, cannot be considered as the practical solution.

In the classical approach discussed above, only P_4 vectors in α-ß subspace are used, however, the availability of the relatively large number of voltage vectors creates opportunities to further improve torque and flux steady-state and dynamic behavior, while suppressing current harmonics. In order to achieve better performance, it is necessary to consider both α-β and x-y subspaces while selecting voltage vectors.

Therefore, both P_4 and P_3 vectors in the α-β subspace are considered in [16],[20]. For example, if the stator flux vector $\Psi_{\alpha\beta}$ lies in Sector I and both torque and stator flux amplitude

need to be increased, the candidate vectors are V_{27} and V_{10} which are in phase in the α-β subspace, as can be seen in Fig. 4. These two vectors have similar effects on torque generation. On the contrary, these two vectors are out of phase in the x-y subspace and have an opposite effect on flux in the x-y subspace. The voltage vector which can reduce the length of flux in x-y subspace will be selected from V_{27} and V_{10}, since the flux in x-y subspace presents the major source of current harmonics in x-y subspace.

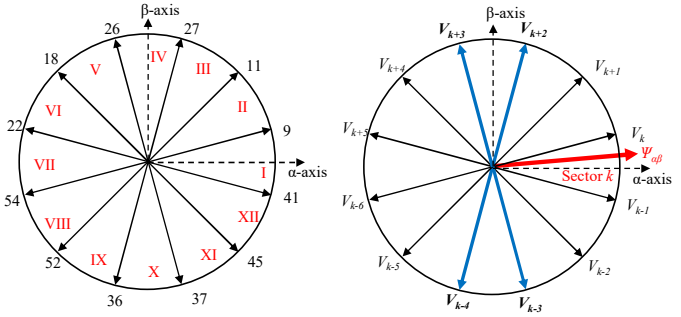

Fig. 3 Classical ST-DTC of dual 3-ph PMSM. (a) 12 sectors in α-β subspace. (b) Voltage vector selection when the flux is in Sector *k*.

TABLE I
SWITCHING TABLE OF CLASSICAL ST-DTC
(with reference to Fig. 4(b) when $\Psi_{\alpha\beta}$ is in Sector *k*)

Sector *k*	$T_e\uparrow$	$T_e\downarrow$
$\Psi_{\alpha\beta}\uparrow$	V_{k+2}	V_{k-3}
$\Psi_{\alpha\beta}\downarrow$	V_{k+3}	V_{k-4}

Following the same principle of reducing the amplitude of the x-y stator flux vector, as discussed above, the synthetic vector ST-DTC is developed in [21]. The 12 synthetic vectors forming dodecagon P_{syn} are shown in Fig. 4. These vectors can be used directly by replacing the vectors from dodecagon P_4 in the classical ST-DTC. P_{syn} vectors are formed from P_4 and P_3 vectors in the α-β subspace (they appear as P_1 and P_3 vectors in the x-y subspace, respectively). Using the same example as above, vector V_{27} from dodecagon P_4 and vector V_{10} from dodecagon P_3 are selected, as shown in Fig. 4. As discussed above these two vectors are in phase in the α-β subspace and have a similar effect on the torque and α-ß stator flux amplitude, while they are in phase opposition in the x-y subspace. If both of these two vectors are applied in one sampling period, by adjusting their dwell times, zero average voltage in x-y subspace can be obtained, and in that x-y current harmonics can be reduced, as can be seen from (1) and (2).

In the synthetic ST-DTC, the average x-y voltage is thus set to zero (within one sample period) by adjusting the dwell times of selected voltage vectors as in (5),

$$\begin{cases} L_{P3}\cdot T_{P3\_xy} - L_{P1}\cdot T_{P1\_xy} = 0 \\ T_{P3\_xy} + T_{P4\_xy} = T_s \end{cases} \tag{5}$$

where T_{P3_xy}, T_{P1_xy} are the dwell times of P_3 and P_1 vectors in the x-y subspace, respectively, and L_{P3} and L_{P1} are amplitudes of these vectors as defined in (4). From (4) and (5) the dwell times of P_4 and P_3 vectors in α-β subspace are obtained as in (6). The amplitude of P_{syn} vectors in the α-β subspace is given by (7). It should be highlighted that the synthetic vector ST-DTC approaches available in the literature such as above discussed [21]-[22] can only eliminate current harmonics caused by uncontrolled x-y voltage by maintaining zero average voltage in x-y subspace. However, they cannot provide compensation for inherent system harmonics, for example, dead-time and distorted back-emf, which are in x-y subspace.

$$\begin{cases} T_{P4\_\alpha\beta} = T_{P1\_xy} = \dfrac{2\sqrt{2}}{\sqrt{6}+\sqrt{2}}\cdot T_s \\ T_{P3\_\alpha\beta} = T_{P3\_xy} = \dfrac{\sqrt{6}-\sqrt{2}}{\sqrt{6}+\sqrt{2}}\cdot T_s \end{cases} \tag{6}$$

$$L_{P_{syn}} = \frac{L_{P4}\cdot T_{P4\_\alpha\beta} + L_{P3}\cdot T_{P3\_\alpha\beta}}{T_s} = \frac{3\sqrt{2}-\sqrt{6}}{3}\cdot V_{DC} \tag{7}$$

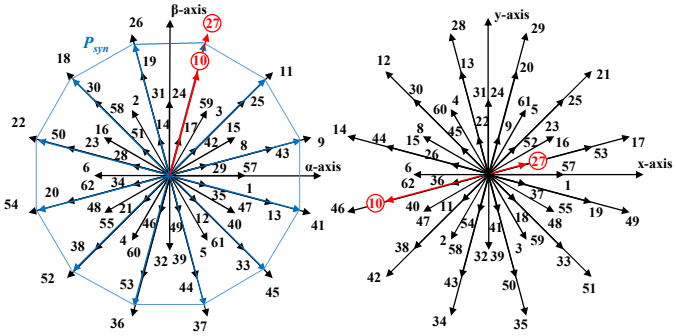

Fig. 4 Synthetic vector ST-DTC [21].

IV. PROPOSED ST-DTC WITH CLOSED-LOOP CURRENT HARMONICS COMPENSATION

The block diagram of the proposed ST-DTC for dual 3-ph PMSMs is shown in Fig. 5(a) with the inclusion of the x-y current harmonics closed-control loop and modified switching table. The x-y current controller provides the reference x-y voltage, which is the input to the switching table, as shown in Fig. 5(a). Therefore, based on torque and stator flux requirements, voltage vectors are selected in the α-β subspace and the dwell times of these vectors are determined in the x-y subspace based on the modulation of the x-y voltage references (provided by the x-y current loop) that need to be injected into the machine voltages in order to reduce stator current harmonic distortion. The steps involved in developing the modified switching table are shown in Fig. 5 (b) with the accompanying detailed explanation included in this section. This can compensate for stator current harmonics caused by various sources, such as dead-time, back-emf, and stator winding asymmetries.

The following parts are organized with reference to Fig. 5 (b). Voltage vectors are explained firstly in Section IV.A, followed by the introduction of PIR controllers in Section IV.B, whose outputs are the voltage references in x-y subspace. Then, the calculation of dwell times of voltage vectors and the optimization of duty cycles are illustrated in Section IV.C and IV.D, respectively.

A. *Selection of Voltage Vectors*

In the proposed ST-DTC, instead of selecting one voltage vector as in the classical ST-DTC, or two voltage vectors as in the synthetic vector ST-DTC [21], one group of three voltage vectors is employed in one sampling period. In order to modulate the (non-zero) x-y voltage references generated from the current controllers at least three voltage vectors are required. Vector groups are decided in the α-β subspace while considering their corresponding mapping in the x-y subspace. In order to modulate a rotating x-y voltage vector (provided by the x-y current loop), three voltage vectors located in three different quadrants in the x-y subspace are required. Two sets of such vector groups can be identified. One vector group from each set is shown in α-β and x-y subspaces in Fig. 6(a) and (b), respectively, for the case when $\Psi_{\alpha\beta}$ lies in Sector I.

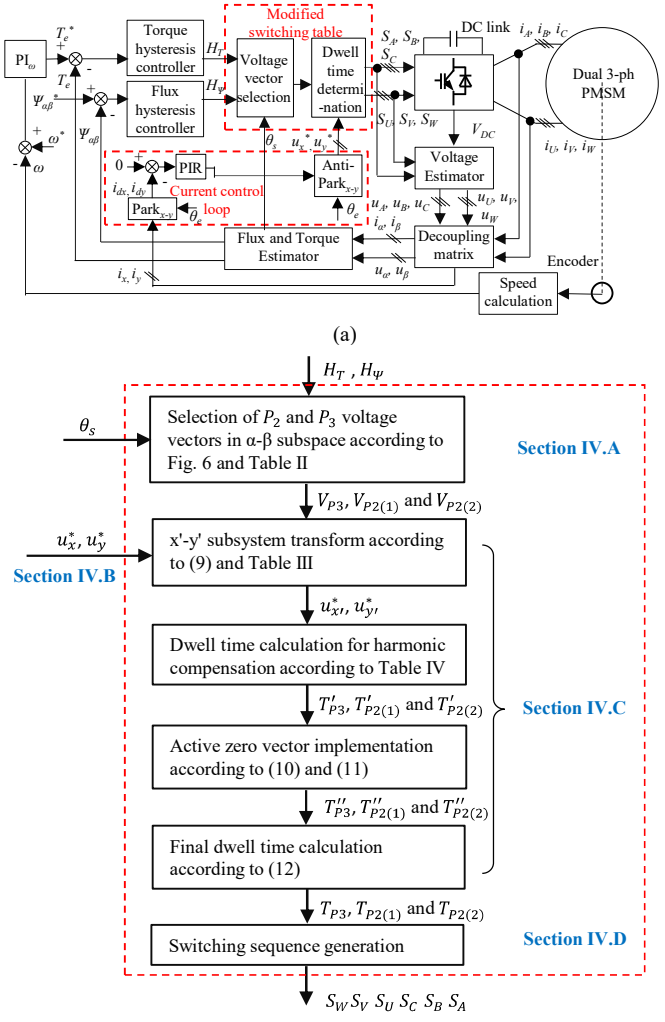

Fig. 5 Proposed ST-DTC of dual 3-ph PMSMs integrating closed-loop current harmonics compensation. (a) Control block diagram. (b) Details of modified switching table.

The first set includes vector groups of three adjacent voltage vectors from dodecagon P_4 in the α-β subspace, which are mapped into P_1 dodecagon in the x-y subspace, as denoted by circles in Fig. 6(a) and (b), for one vector group when $\Psi_{\alpha\beta}$ lies in Sector I. Vector groups from this set will lead to the large inverter DC link voltage utilization as only large vectors are employed in the α-β subspace. However, it will result in relatively small x-y voltages that can be modulated by small P_1 vectors in the x-y subspace.

The second set includes vector groups of three adjacent vectors with two vectors from dodecagon P_2 and one vector from dodecagon P_3 in the α-β subspace, which are mapped into P_1 and P_3 vectors in the x-y subspace, respectively, as denoted by rectangles in Fig. 6(a) and (b), for one vector group when $\Psi_{\alpha\beta}$ lies in Sector I. This will lead to the small DC link voltage utilization, but larger available x-y voltages in comparison with the first set. The second set of voltage vectors is implemented in this work. It should be noted that P_2 vectors have two redundant switching states, whereby either can be used. All the 12 vector groups (of the second set) are listed in Table III.

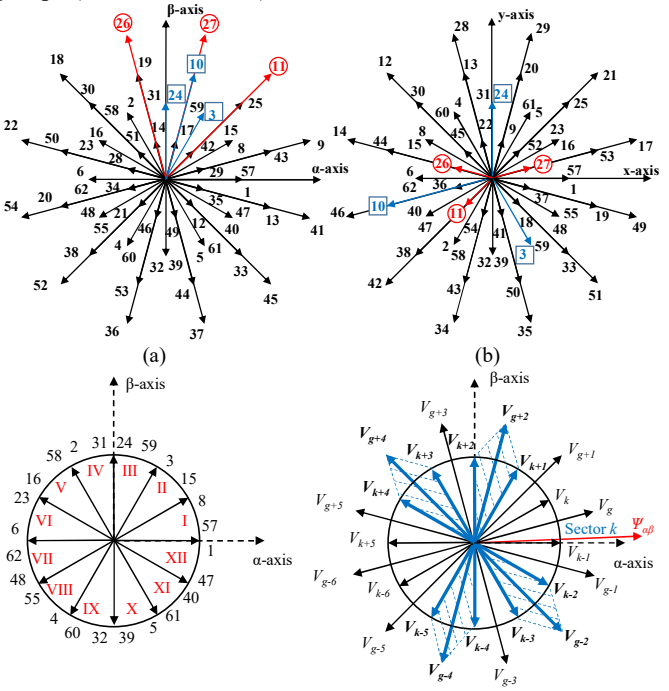

Fig. 6 Regulation principle of proposed ST-DTC. (a) Voltage vector group in α-β subspace. (b) Voltage vector group in x-y subspace. (c) 12 sectors in α-β subspace. (d) Vector selection when the flux is in Sector *k*.

In the proposed approach, the α-β subspace is divided into 12 sectors using voltage vectors from dodecagon P_2 as boundaries (in the classical approach P_1 vectors are used as the boundaries), as shown in Fig. 6(c), while sectors are selected based on the position of the stator flux vector (as in the classical approach). The selection of vector groups is based on the outputs of torque and flux hysteresis controllers and is defined by Table II and Fig. 6(d).

In general, if $\Psi_{\alpha\beta}$ is located in Sector k ($k = \mathrm{I}, \mathrm{II}, .. \mathrm{XII}$), 4 possible groups can be used, as shown in Fig. 6(d) (where the vectors from dodecagon $P_2$are denoted by subscript "k" and the vectors from dodecagon P_3 are denoted by subscript "g"). Groups 1 to 4 are centered about vectors $V_{g+2}, V_{g+4}, V_{g-4}$ and

V_{g-2}, respectively, where vector V_g is in Sector k, as can be seen from Fig. 6(d).

In particular, when $\Psi_{\alpha\beta}$ is in Sector I, the group of V_3, V_{24}, V_{10} and the group of V_{30}, V_{58}, V_{23} will increase torque, while the group of V_{44}, V_{32}, V_{61} and the group of V_{53}, V_{60}, V_{39} will decrease torque. This can be identified from Table II and Fig. 6(a) and Fig. 6(d). Also, the group of V_{33}, V_5, V_{40} and the group of V_3, V_{24}, V_{10} will result in an increase in the flux amplitude, while the group of V_{30}, V_{58}, V_{23} and the group of V_{53}, V_{60}, V_{39} will results in an decrease in the flux amplitude. One vector group is then selected based on the signs of the torque and flux amplitude errors. These are provided by the torque and flux hysteresis controllers, respectively, as shown in Fig. 5(a).

TABLE II
SWITCHING TABLE OF PROPOSED ST-DTC
(with reference to Fig. 6(d) when $\Psi_{\alpha\beta}$ is in Sector k)

Sector k	$T_e\uparrow$	$T_e\downarrow$
$\Psi_{\alpha\beta}\uparrow$	V_{k+1}, V_{k+2}, V_{g+2}	V_{k-2}, V_{k-3}, V_{g-2}
$\Psi_{\alpha\beta}\downarrow$	V_{k+3}, V_{k+4}, V_{g+4}	V_{k-4}, V_{k-5}, V_{g-4}

B. Current Controllers in x-y Subspace

The x-y current closed-control loops with proportional-integral-resonant (PIR) controllers are included in the proposed ST-DTC structure, as shown in Fig. 5(a). In this structure, the outputs of the current control loops are x-y voltage references (denoted by u_x^* and u_y^* in Fig. 5) which are used in the (online) calculation of dwell times of selected voltage vectors. Since the purpose of the added x-y current control loop is to suppress current harmonics, the x-y current references are set to zero. The x-y currents are transformed into the equivalent rotating reference frame, that rotates at the angular speed of the stator currents. In this reference frame, the 5th and 7th order harmonics, which are normally dominant stator current harmonics and are mapped into the x-y subspace, will appear as the 6th order harmonic [26]. One type of PIR controllers [34]-[35] given by (8), are tuned to suppress the 6th harmonic, where K_p and K_i are proportional and integral gains, K_r is resonant gain, h is harmonic order ($h = 6$), and ω_s and ω_c denote fundamental frequency and the cut-off frequency, respectively.

$$\begin{cases} G_{PIR}(s) = K_p + \dfrac{K_i}{s} + G_R(s) \\ G_R(s) = \dfrac{K_r s}{s^2 + \omega_c s + (h\omega_s)^2} \end{cases} . \tag{8}$$

Matlab optimization tool is used for PIR tuning. K_r can be set to be the same as (or around) K_i [25]-[26], [35]. The cut-off frequency ω_c can be used to increase the bandwidth at the resonant frequency to reduce the sensitivity of the resonant controller [35]. The bode diagram with different ω_c at K_r=1849.6 is shown in Fig. 7, from which a larger ω_c leads to a wider bandwidth and a smaller gain at the resonant frequency. According to Fig. 7, ω_c can be tuned through online adjustment [25]-[26], [35].

C. Dwell Time Determination

As stated before, the dwell times of selected voltage vectors are determined in the x-y subspace based on the outputs of the x-y current loops. The aim here is to modulate the reference x-y voltages (obtained from the x-y current loops) using voltage vectors mapped into the x-y subspace. In order to simplify the process of determining the dwell times of selected vectors, a new reference frame is introduced, and hereinafter termed the x'-y' subsystem, where x'-axis is aligned with P3 vector of the selected vector group. Without this new reference frame, dwell time calculation for each voltage vector group cannot be unified, resulting in massive computation, since each voltage vector group has a different location with reference to x-axis and y-axis. Thus, the new x'-y' subsystem is introduced to unify the calculation of dwell times of all the voltage vector groups. Taking one group of three voltage vectors, for example, the group of V_{10}, V_3 and V_{24}, the direction of x'-axis is determined by V_{10}, as shown in Fig. 8(a). The y'-axis is then set to lag the x'-axis by 90°. For the other vector groups (listed in Table III) the same approach is employed in defining the x'-y' subsystem.

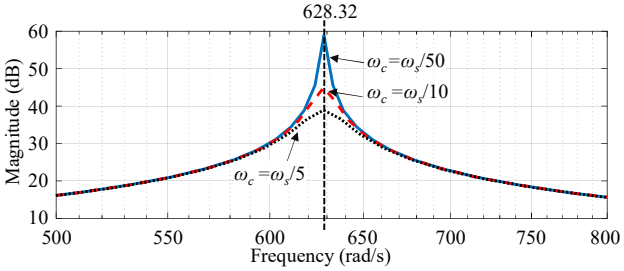

Fig. 7 Bode diagram of G_R(s) with $\omega_c = \omega_s/5$, $\omega_s/10$ and $\omega_s/50$, respectively, with $\omega_s = 104.72$ rad/s and h=6.

TABLE III
ANGLE γ DENOTED IN FIG. 8(A) FOR TRANSFORMATION OF X-Y VOLTAGES TO X'-Y' SUBSYSTEM

Voltage vector group	γ	Voltage vector group	γ
V_{10}, V_3, V_{24}	$\frac{11}{12}\pi$	V_{53}, V_{60}, V_{39}	$\frac{23}{12}\pi$
V_{19}, V_{31}, V_2	$\frac{1}{12}\pi$	V_{44}, V_{32}, V_{61}	$\frac{13}{12}\pi$
V_{30}, V_{58}, V_{23}	$\frac{5}{4}\pi$	V_{33}, V_5, V_{40}	$\frac{1}{4}\pi$
V_{50}, V_{16}, V_{62}	$\frac{5}{12}\pi$	V_{13}, V_{47}, V_1	$\frac{17}{12}\pi$
V_{20}, V_6, V_{48}	$\frac{19}{12}\pi$	V_{43}, V_{57}, V_{15}	$\frac{7}{12}\pi$
V_{38}, V_{55}, V_4	$\frac{3}{4}\pi$	V_{25}, V_8, V_{59}	$\frac{7}{4}\pi$

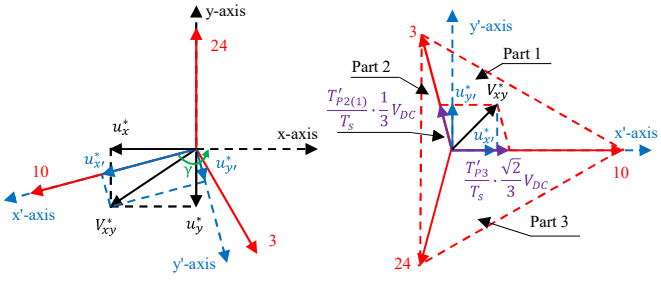

(a) (b)

Fig. 8 Dwell times of selected vectors in proposed ST-DTC. (a) Establishment of x'-y' subsystem. (b) Modulation of x-y voltage in x'-y' subsystem.

The next step in determining the dwell times of selected vectors is to transform the x-y reference voltages into the x'-y' subsystem, denoted by $u_{x'}^*$ and $u_{y'}^*$ in Fig. 8. The transformation is given by (9) in which γ is the angel from x'-axis to x-axis in the anti-clockwise direction. For the group of V_{10}, V_3 and V_{24}, γ is $\frac{11}{12}\pi$. The angle γ for each vector group is listed in Table III.

$$\begin{cases} u_{x'}^* = \cos(\gamma)\cdot u_x^* + \cos(\gamma+\frac{1}{2}\pi)\cdot u_y^* \\ u_{y'}^* = \sin(\gamma)\cdot u_x^* + \sin(\gamma+\frac{1}{2}\pi)\cdot u_y^* \end{cases} \tag{9}$$

The dwell times are then calculated using $u_{x'}^*$ and $u_{y'}^*$ voltages, as shown in Fig. 8(b) for the vector group of V_{10}, V_3 and V_{24}. The x'-y' plane is divided into the three triangles, namely, Part 1 bounded by V_{10} and V_3, Part 2 bounded by V_3 and V_{24}, and Part 3 bounded by V_{24} and V_{10}. When reference x-y voltage (denoted by V_{xy}^* in Fig. 8) is in Part 1, it is modulated by V_{10} and V_3. Meanwhile, V_{xy}^* is synthesised by V_3 and V_{24} in Part 2, and by V_{24} and V_{10} in Part 3. Table IV shows separately the dwell times expressions of selected voltage vectors when V_{xy}^* is in Part 1, Part 2 and Part 3, where T'_{P3} denotes the dwell time of the vector from dodecagon P_3, while $T'_{P2(1)}$ and $T'_{P2(2)}$ are the dwell times of the two vectors from dodecagon P_2 (where $V_{P2(2)}$ lags $V_{P2(1)}$ by 120°). The dwell times expressions in Table IV are the same for any vector group from Table III.

TABLE IV
DWELL TIMES OF V_{P3}, $V_{P2(1)}$ AND $V_{P2(2)}$

	Dwell times of V_{P3}, $V_{P2(1)}$ and $V_{P2(2)}$
Part 1	$T'_{P3} = \frac{3T_s}{\sqrt{2}V_{DC}\cos\frac{\pi}{12}}(\cos\frac{\pi}{12}u_{x'}^* + \sin\frac{\pi}{12}u_{y'}^*)$
	$T'_{P2(1)} = \frac{3T_s}{V_{DC}\cos\frac{\pi}{12}}u_{y'}^*$
	$T'_{P2(2)} = 0$
Part 2	$T'_{P3} = 0$
	$T'_{P2(1)} = \frac{3T_s}{2V_{DC}}(-\frac{u_{x'}^*}{\sin\frac{\pi}{12}} + \frac{u_{y'}^*}{\cos\frac{\pi}{12}})$
	$T'_{P2(2)} = \frac{3T_s}{2V_{DC}}(-\frac{u_{x'}^*}{\sin\frac{\pi}{12}} - \frac{u_{y'}^*}{\cos\frac{\pi}{12}})$
Part 3	$T'_{P3} = \frac{3T_s}{\sqrt{2}V_{DC}\cos\frac{\pi}{12}}(\cos\frac{\pi}{12}u_{x'}^* - \sin\frac{\pi}{12}u_{y'}^*)$
	$T'_{P2(1)} = 0$
	$T'_{P2(2)} = \frac{3T_s}{V_{DC}\cos\frac{\pi}{12}}(-u_{y'}^*)$

Furthermore, if $T'_{P3} + T'_{P2(1)} + T'_{P2(2)} < T_s$, one active zero vector (AZV) [36]-[38], can be implemented in the x-y subspace to maximize the α-β voltages. The employed AZV comprises all vectors from the selected vector group, i.e. one P_3 vector and two P_2 vectors. The dwell times T''_{P3}, $T''_{P2(1)}$ and $T''_{P2(2)}$ of vectors V_{P3}, $V_{P2(1)}$ and $V_{P2(2)}$, respectively, that form one AZV, can be obtained from (10) (with reference to Fig. 8(b)). AZV can increase the dwell times of selected voltage vectors, while it does not affect the x-y voltages. Therefore, α-β voltage amplitude can be increased and the DC link voltage utilization can be improved.

Dwell times T''_{P3}, $T''_{P2(1)}$ and $T''_{P2(2)}$ are then given by (11), while the total dwell times of selected vectors V_{P3}, $V_{P2(1)}$ and $V_{P2(2)}$, after introducing AZV, are given by (12). The α-β voltage vector $V_{\alpha\beta\_AZV}$ obtained after implementing AZV in the x-y subspace, is aligned with the P_3 vector in the selected vector group and its amplitude is given by (13).

$$\begin{cases} 0 = L_{P3}\cdot T''_{P3} - \sin\frac{\pi}{12}\cdot L_{P2}\cdot(T''_{P2(1)} + T''_{P2(2)}) \\ 0 = \cos\frac{\pi}{12}\cdot L_{P2}\cdot T''_{P2(1)} - \cos\frac{\pi}{12}\cdot L_{P2}\cdot T''_{P2(2)} \\ T''_{P3} + T''_{P2(1)} + T''_{P2(2)} = T_s - T'_{P3} - T'_{P2(1)} - T'_{P2(2)} \end{cases} \tag{10}$$

$$\begin{cases} T''_{P3} = \dfrac{\sin\frac{\pi}{12}}{\sin\frac{\pi}{12}+\sqrt{2}}(T_s - T'_{P3} - T'_{P2(1)} - T'_{P2(2)}) \\ T''_{P2(1)} = T''_{P2(2)} \\ \qquad = \dfrac{\sqrt{2}}{2\sin\frac{\pi}{12}+2\sqrt{2}}(T_s - T'_{P3} - T'_{P2(1)} - T'_{P2(2)}) \end{cases} \tag{11}$$

$$\begin{cases} T_{P3} = T'_{P3} + T''_{P3} \\ T_{P2(1)} = T'_{P2(1)} + T''_{P2(1)} \\ T_{P2(2)} = T'_{P2(2)} + T''_{P2(2)} \end{cases} \tag{12}$$

$$\begin{aligned} |V_{\alpha\beta_{AZV}}| = {} & \frac{\sqrt{2}V_{DC}}{3}\cdot\frac{T''_{P3}}{T_s} + \frac{V_{DC}\cos\frac{\pi}{12}}{3}\cdot\frac{T''_{P2(1)}}{T_s} \\ & + \frac{V_{DC}\cos\frac{\pi}{12}}{3}\cdot\frac{T''_{P2(2)}}{T_s} \end{aligned} \tag{13}$$

D. Switching Sequence Generation

The voltage vectors with their dwell times are delivered to the machine by the switching sequence of each phase during each sampling period. The standard optimization approach to minimize the number of commutations per phase and to simplify microcontroller implementation is adopted. For completeness, the main steps are included in this section.

One original switching sequence $V_{10}V_{24}V_3$ is shown in Fig. 9(a) for the vector group of V_{10}, V_3 and V_{24} with their dwell time calculated from (12), for example, $T_{24} > T_{10} > T_3$. From Fig. 9(a), Phase B experiences multiple switching per sampling period. For instance, the total turn-on time of Phase B is divided into two segments, shadowed in Fig. 9(a), creating two turn-on and two turn-off events. If the switching sequence is arranged as $V_{24}V_{10}V_3$, this multiple switching problem can be solved. However, the specific switching sequence order for each group complicates the generation procedure. On the other hand, the switching sequence is not symmetric regarding the middle of each sampling period, which means a complex logic to generate switching time points for microcontrollers.

Thus, the original switching sequence should be optimized and the steps can be summarized as 1) Calculate the total turn-on time of each phase during each sampling period; 2) Centralize the total turn-on time of each phase in each sampling period; 3) Generated the switching sequence. The optimization aim is to avoid the multiple switching and to achieve the symmetric switching sequence in each sampling period. These

steps are explained in detail still with the vector group of V_{10}, V_3 and V_{24} with $T_{24} > T_{10} > T_3$, the same as Fig. 9(a).

Firstly, the total turn-on time for each phase can be in general calculated by (14) from Table IV and (10)-(12). Secondly, an optimized switching sequence with the symmetric arrangement in one sampling period can be generated by simply arranging the total turn-on time of each phase (presented in (14)) in the middle of the sampling period, shown in Fig. 9(b). For Phase A, the turn-on and turn-off instances happen at the time points $\frac{T_s-T_{on\_A}}{2}$ and $\frac{T_s+T_{on\_A}}{2}$ in each sampling period, respectively. The same rule for the turn-on and turn-off instances applies to other phases. It can be seen that the two-segment turn-on time of Phase B in Fig. 9(a) appears as one total turn-on time in the middle, shadowed in Fig. 9(b). Finally, the optimized voltage vector order is given by $V_0V_8V_{26}V_{27}V_{26}V_8V_0$. After optimization, there are no multiple switches in each phase and the symmetric switching sequence without complicated switching logic is generated.

$$\begin{cases} T_{on\_A} = T_3 \\ T_{on\_B} = (T_{10} + T_3) \\ T_{on\_C} = 0 \\ T_{on\_U} = (T_{10} + T_{24}) \\ T_{on\_V} = T_{24} \\ T_{on\_W} = 0 \end{cases} \tag{14}$$

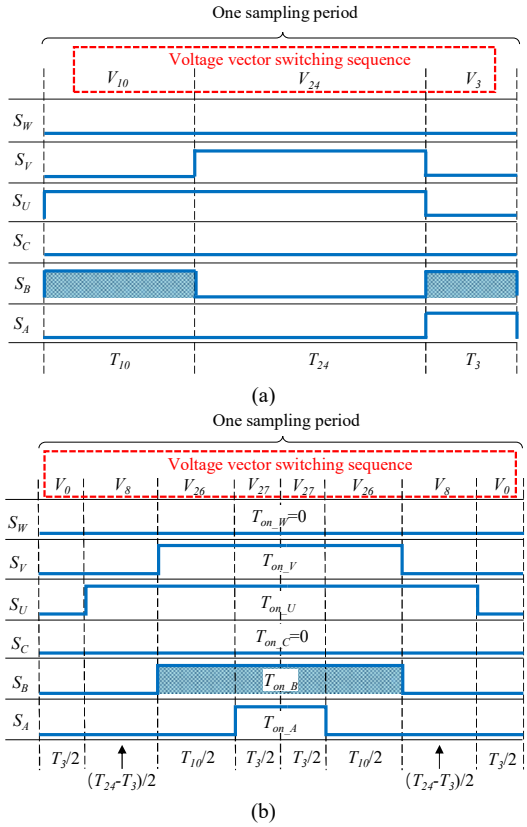

Fig. 9 Switching sequence for voltage vector group of V_{10}, V_3 and V_{24}. (a) Original. (b) Optimized.

The equivalence of the original and optimized switching sequences regarding the modulated (or resulting) voltages in two subspaces should be assured. Then, Fig. 10 further illustrates that the original switching sequence shown in Fig. 9(a) and the optimized switching sequence shown in Fig. 9(b) produce the same $V_{\alpha\beta}$ and V_{xy}. It is because the average voltage of each phase during each sampling period reflecting the modulation of $V_{\alpha\beta}$ and V_{xy} does not change with the same total turn-on time. The only difference is the allocation of the total turn-on time of each phase. It should be noted that for different combinations of T_3, T_{10} and T_{24}, the optimized switching sequence may be different but the produced V_{xy} and $V_{\alpha\beta}$ voltages remain the same as the original switching sequence. For other voltage vector groups, the same optimization procedure applies.

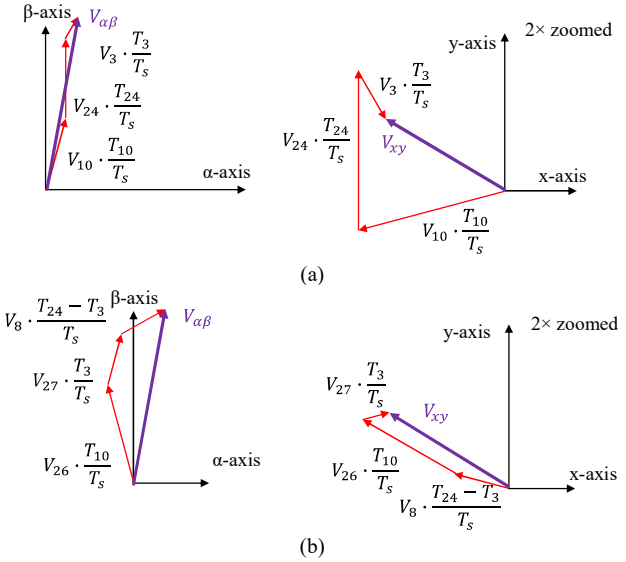

Fig. 10 Resulting vectors in α-β and x-y subspaces (The voltage vector length in x-y subspace is zoomed-in 2×, compared with that in α-β subspace.). (a) Original switching sequence regarding Fig. 9(a). (b) Optimized switching sequence regarding Fig. 9(b).

V. Analysis of DC Link Voltage Utilization for Proposed ST-DTC

This section investigates the DC link voltage utilization of the VSI, when the proposed ST-DTC is employed. The DC link voltage utilization rate is expressed here as the ratio of the $V_{\alpha\beta}$ amplitude to the P_4 vector amplitude (L_{P4}), as given by (15), and gives a measure of machine torque that can be produced for the inverter DC link voltage.

In the proposed approach, the α-β and x-y subspaces are coupled through the dwell times of selected voltage vectors; in that, it is important to express $V_{\alpha\beta}$ as a function of V_{xy}, as is provided by (16) for the vector group of V_{10}, V_3 and V_{24}. The DC link voltage utilization rate can then be expressed as a function of V_{xy}, as given by (18), by substituting (16) into (15). From (18), when V_{xy} is zero, the utilization rate η is 0.535. However, for non-zero V_{xy} voltage, the η is not constant as it changes as the vector V_{xy} rotates (in the x-y subspace), as is shown in Fig. 11 for the vector group of V_{10}, V_3 and V_{24}, where the constant η contours are plotted by using (18). The radius of the inscribed circle in the triangle (bounded by vectors V_{10}, V_3 and V_{24}) in Fig.

11 presents the maximum amplitude of the x-y voltage that can be modulated in the linear range and is the same for any vector group from Table III. The V_{xy} amplitude can be obtained from Fig. 11 and is given by (17).

$$\eta = \frac{|V_{\alpha\beta}|}{L_{P4}} = \frac{\sqrt{u_\alpha^2 + u_\beta^2}}{\frac{\sqrt{6}+\sqrt{2}}{6} V_{DC}} \tag{15}$$

$$\begin{cases} u_\alpha = \dfrac{3\sqrt{2}-\sqrt{6}}{12+8\sqrt{3}} u_{x'} + \dfrac{3\sqrt{2}+\sqrt{6}}{12+8\sqrt{3}} u_{y'} + \dfrac{1}{6+3\sqrt{3}} V_{DC} \\ u_\beta = \dfrac{3\sqrt{2}+\sqrt{6}}{12+8\sqrt{3}} u_{x'} - \dfrac{3\sqrt{2}-\sqrt{6}}{12+8\sqrt{3}} u_{y'} + \dfrac{1}{3} V_{DC} \end{cases} \tag{16}$$

$$0 \le |V_{xy}| \le \frac{V_{DC} \sin\left(\frac{\pi}{12}\right)}{3} \tag{17}$$

$$\eta = \frac{0.416\sqrt{(u_{x'} + 1.29V_{DC})^2 + (u_{y'})^2}}{V_{DC}} \tag{18}$$

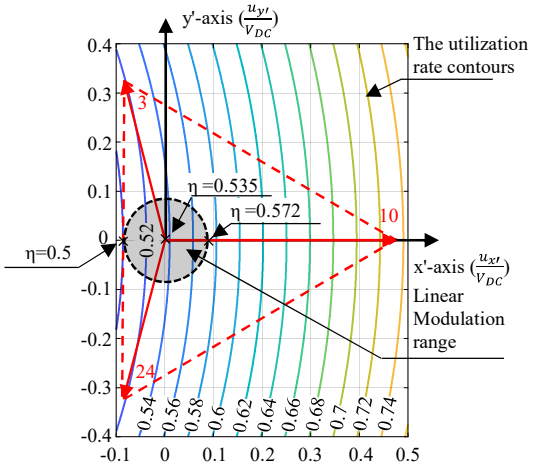

Fig. 11 Utilization rate contours in x'-y' subsystem for proposed ST-DTC.

The coupling between the x-y and α-β subspaces is further demonstrated in Fig. 12, by again considering the vector group of V_{10}, V_3 and V_{24}. However, this applies to any of the 12 vector groups in Table III. It shows that as the V_{xy} rotates in the x-y subspace, with the amplitude of ε (where $0 < \varepsilon \le \frac{1}{3} V_{DC} \sin\left(\frac{\pi}{12}\right)$), the $V_{\alpha\beta}$ also rotates in the α-β subspace with the amplitude of r (where $r = \frac{\sqrt{2}}{2\sqrt{3}+4}\varepsilon$) about the point that corresponds to the peak of $V_{\alpha\beta}$ when $\varepsilon = 0$. For the vector group of V_{10}, V_3 and V_{24}, this point is given by ($u_\alpha = \frac{2-\sqrt{3}}{3} V_{DC}$, $u_\beta = \frac{1}{3} V_{DC}$).

For $\varepsilon = 0$ the $V_{\alpha\beta}$ vector is aligned with the P_3 vector in the α-β subspace and its amplitude is $|V_{\alpha\beta}| = \frac{\sqrt{6}-\sqrt{2}}{3} V_{DC}$, which leads to the utilization rate η of 0.535, as mentioned above. While for $\varepsilon \neq 0$, the η is not constant and, for example, when $\varepsilon = \frac{1}{3} V_{DC} \sin\left(\frac{\pi}{12}\right)$ (maximum x-y voltage in the linear range), the η varies from 0.5 to 0.572 for one full rotation of V_{xy}, as shown in Fig. 12.

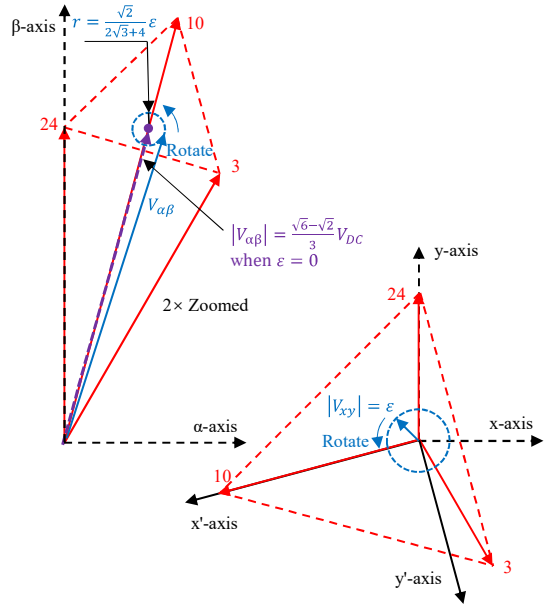

Fig. 12 Relationship of $V_{\alpha\beta}$ and V_{xy} for proposed ST-DTC. (a) $V_{\alpha\beta}$ in α-β subspace. (b) V_{xy} in x-y subspace.

In order to increase the utilization rate, the other set of vector groups, termed 'the first set' in Section IV.A, can be incorporated in the proposed ST-DTC instead of 'the second set'. It includes the groups of three adjacent voltage vectors from dodecagon P_4 which are mapped into P_1 dodecagon in the x-y subspace (as denoted by circles in Fig. 6(a) and (b) for the vector group of V_{27}, V_{11} and V_{26}). This vector group is again presented in Fig. 13 where the constant η contours are plotted (using (19)) together with the inscribed circle in the triangle bounded by the three selected vectors. The radius of the inscribed circle defines the maximum amplitude of the V_{xy} in the linear range and is given as $\varepsilon = \frac{\sqrt{6}-\sqrt{2}}{6} V_{DC} \sin\left(\frac{\pi}{12}\right)$, which is ~two times smaller than when the vector groups from Table III are used.

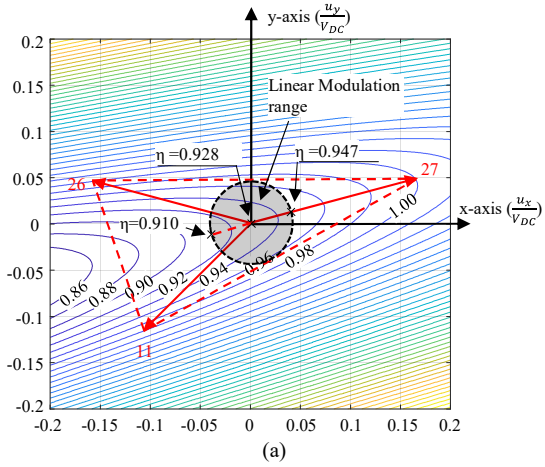

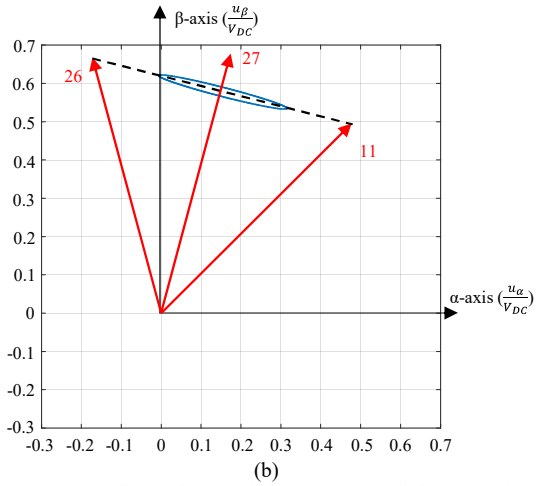

(b)

Fig. 13 Vector group denoted by circles in Fig. 6(a) and (b). (a) Utilization rate contours in the x-y subspace. (b) Trajectory of $V_{\alpha\beta}$ for one full rotation of V_{xy}.

Although the $V_{\alpha\beta}$ amplitude is significantly increased when P_4 vectors are used, close attention should be paid to the phase angle of the vector $V_{\alpha\beta}$, as it can deviate up to $\sim \frac{\pi}{12}$ degrees from the middle vector (V_{27} in this vector group) for one full rotation of V_{xy}, as can be seen in Fig. 13(b), which might pose challenges for the torque and flux control in the α-β subspace. This analysis is however beyond the scope of this paper.

$$\eta = \frac{\sqrt{\left(u_x - 3.46u_y + 0.155V_{DC}\right)^2 + \left(u_y + 0.577V_{DC}\right)^2}}{0.644V_{DC}} \quad (19)$$

Nevertheless, in order to increase the inverter DC link voltage utilization, one set of vector groups with larger vectors is required, for example synthetic vectors as in [21] or P_4 vectors, in addition to the set of vector groups in Table III, and the selection between the two sets can be decided based on the torque error and multi-level hysteresis torque controller. This hybrid approach is well established in the literature and is commonly employed in order to achieve torque ripple reduction as in [22]. This will be part of our future investigation and is out of scope of this paper.

VI. Experimental Results

The effectiveness of the proposed ST-DTC strategy is verified experimentally on a VSI-fed dual 3-ph PMSM laboratory prototype with DSPACE DS1005 control platform. The system parameters are given in Table V. The back-emf of the test machine is shown in Fig. 14(a) for the speed of 200 r/min. It can be seen in Fig. 14 (b) that the back-emf is distorted with dominant 5th and 7th harmonics (3rd harmonics are inherently canceled in the 3-ph system) which together with the inverter nonlinearities cause the 5th and 7th stator current harmonics. In order to demonstrate the advances of the proposed ST-DTC, the synthetic vector ST-DTC developed in [21] is also implemented on the laboratory prototype, together with the classical ST-DTC which is included for the sake of completeness.

The parameters of the PI controllers are tuned using the Matlab optimization tool, and the parameters listed in Table V provide an overshoot of 2.4% and a rising time of 1.69ms. The resonant gain K_r is selected to be the same as the integrator gain [25]-[26], [35].

TABLE V
Parameters of Testing PMSM and Drive System

Parameters	Value
PM flux linkage	75 mWb
Number of pole pairs	5
Stator resistance	1.10 Ω
α/β-axis inductance	2.14mH
x/y-axis inductance	0.88mH
Rated speed	400 r/min
Rated torque	5.5 Nm
V_{DC}	60V
Sampling frequency	10kHz
Torque bandwidth	0.01
Flux bandwidth	0.0005
PIR K_p	10.2
PIR K_i	1849.6
PIR K_r	1849.6
ω_c	ω_s /50

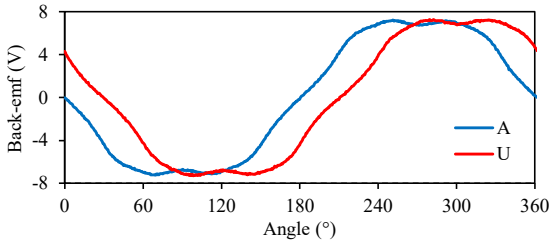

(a)

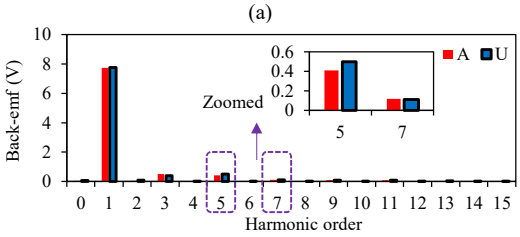

(b)

Fig. 14 Back-emf of test machine. (a) Back-emf waveforms of Phase A and Phase U. (b) Back-emf spectrum analysis.

The experimental results are shown in Fig. 15 where the proposed ST-DTC is compared with the synthetic vector [21] and classical ST-DTC under the operating conditions listed in Table V. Fig. 15 (a) and (b) show the phase U current together with its harmonic spectrum. The results clearly demonstrate the effectiveness of the proposed method in suppressing the 5th and 7th harmonics. The current THD is improved with respect to the synthetic ST-DTC [21], as can be seen from Table VI. The THD improvements with respect to [21] are more evident for larger low-frequency harmonics in the stator current as is shown through simulation in Section VII. This is obtained by controlling the x-y currents to zero as can be seen in Fig. 15 (c) and (d). This is in contrast with [21] where the x-y voltages are set to zero, as is shown in Fig. 16(a). In that, the method in [21] cannot suppress current harmonics caused by machine/inverter non-idealities.

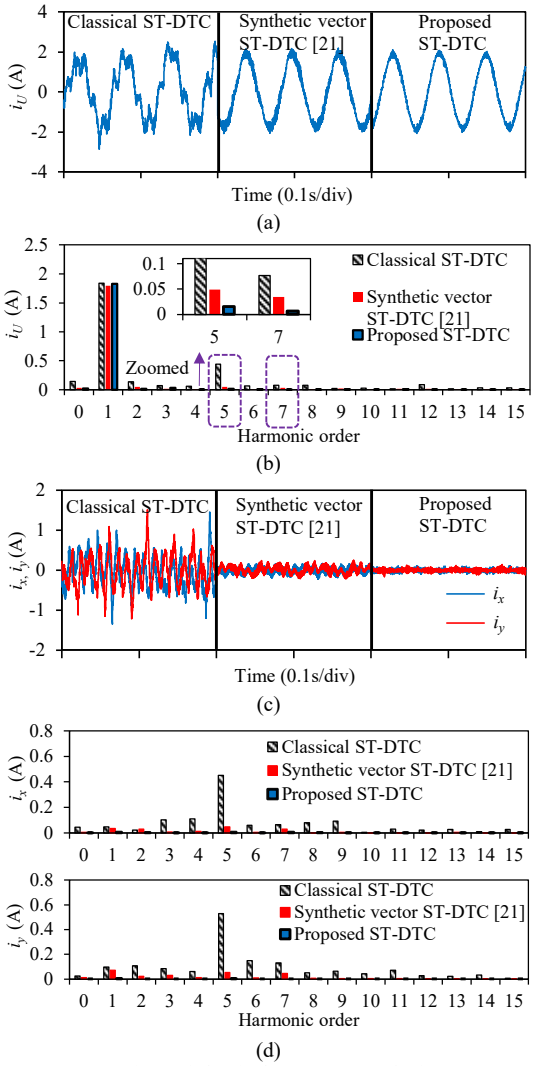

Fig. 15 Current comparison of classical ST-DTC, synthetic vector ST-DTC and proposed ST-DTC. (a) Phase U current. (b) Spectrum analysis of Phase U current. (c) Currents in x-y subspace. (d) Spectrum analysis of currents in x-y subspace.

Further, Fig. 16(b) compares the three methods in the α-β subspace. For the classical ST-DTC, the 12 voltage vectors which are used in the α-β subspace are denoted by triangles. From (4) and Table V, the length of these vectors can be found as $L_{P4} \approx 39$V. For the synthetic vector ST-DTC [21], the 12 synthetic vectors are used instead, as denoted by circles. From (7) and Table V, the length of these vectors is given as $L_{P_{syn}} \approx 36$V. For the proposed ST-DTC, the α-β voltage vectors are denoted by squares. The lengths of these voltage vectors vary and are in the range from ~19V to ~22V, as can be obtained from (15) and Table V.

Fig. 16(c) compares the three methods in the x-y subspace. For the classical ST-DTC, the 12 voltage vectors, which are mapped in the dodecagon P_1 in the x-y subspace, are shown by triangles. These voltages, with the amplitude of ~10V, given by (4) and Table V, excite high x-y current harmonics, as they are limited only by the stator resistance and the x-y inductance of 0.88mH, as given in Table V. For the synthetic vector ST-DTC, voltages u_x and u_y are set to zero, as denoted by the circle in the origin of the x-y subspace. For the proposed ST-DTC, the trajectory of the x-y voltage is shown by the filled area around the origin, where the linear operating range of the x-y voltage is limited by the broken-line circle, and is given by $\frac{1}{3}V_{DC}\sin(\frac{\pi}{12}) = 5.18$V for $V_{DC} = 60$V, as indicated in Fig. 16(c).

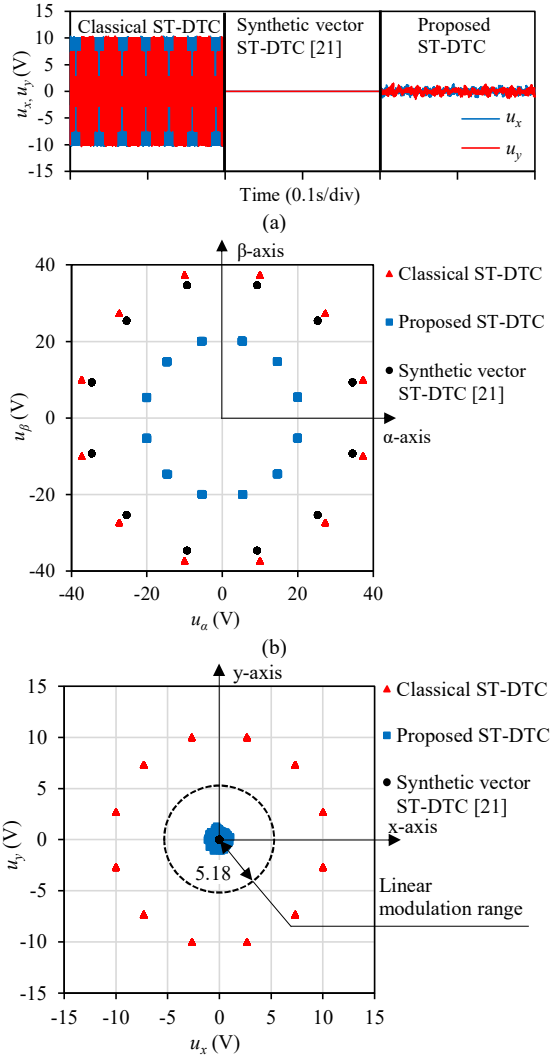

Fig. 16 Voltage comparison of classical ST-DTC, synthetic vector ST-DTC and proposed ST-DTC. (a) Voltage waveforms in x-y subspace. (b) Trajectory of u_α, u_β in α-β subspace. (c) Trajectory of u_x, u_y in x-y subspace.

Fig. 17(a) and (b) show the stator flux and torque for all three methods. It can be seen that the flux and torque ripple are further suppressed by the proposed ST-DTC with respect to [21], as also can be seen from Table VI. This is expected, as in [21] one vector from dodecagon P_4 and one from dodecagon P_3 are used (in one sample period), which result in larger voltage amplitude applied to the machine, with respect to, when two P_2 and one P_3 vectors are used as in the proposed ST-DTC. The comparison of the phase current THD under different loads and different mechanical speed of 200r/min are included in Fig. 18.

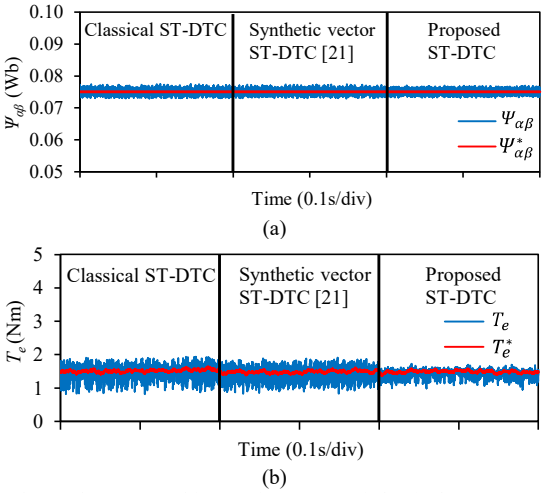

Fig. 17 Flux and torque tracking performances of classical ST-DTC, synthetic vector ST-DTC and proposed ST-DTC. (a) Flux tracking performance. (b) Torque tracking performance.

Meanwhile, in Table VI, the DC link voltage utilization, average switching frequency, the calculating power in dSPACE, and the size of executing files are compared. As illustrated previously, classical and synthetic vector ST-DTC strategies have a similar DC link voltage utilization rate, contributing to approximately the same torque ripple. In terms of the average switching frequency, due to the modulation of voltage references in x-y subspace, the proposed ST-DTC has a larger switching frequency, but still lower than the sampling frequency. It is noted that the switching frequency of PWM techniques is normally the same as the sampling frequency. Thus, the switching losses of the proposed ST-DTC are higher than the other two ST-DTC strategies, but can be still lower than PWM techniques. The proposed ST-DTC requires slightly more calculating power due to the closed-loop current regulation in x-y subspace. Also, the size of the executing file of the proposed ST-DTC is slightly larger than those of the other two strategies.

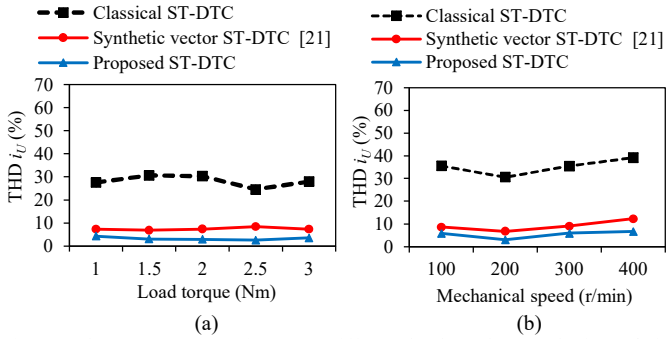

Fig. 18 Phase THD comparison. (a) Different loads at the speed of 200r/min. (b) Different speeds at the load of 1.5 Nm.

The dynamic performances with the mechanical speed changing from 200r/min to 300 r/min with the load of 1.0 Nm for all three ST-DTC strategies are compared in Fig. 19. Furthermore, the dynamic performances with torque changing from 2Nm to 0.5 Nm at the speed of 200r/min are presented in Fig. 20. All three ST-DTC strategies have similar transient performances.

TABLE VI
COMPARISON OF THREE ST-DTC STRATEGIES

	Classical ST-DTC	Synthetic vector ST-DTC [21]	Proposed ST-DTC
$\Psi_{\alpha\beta\_ripple}$ (%)	9.72e-4	9.29e-4	8.08e-4
$T_{e\ ripple}$ (%)	0.251	0.250	0.170
THD of i_U (%)	30.63	7.20	3.07
DC link voltage utilization	1.00	0.928	0.536(avg.)
Average Switching frequency (kHz)	2.58	5.37	9.17
Calculation cycle time (μs)	1.30	1.40	2.00
Compiled object file (.ppc) for execution in dSPACE (KB)	1,160	1,164	1,168

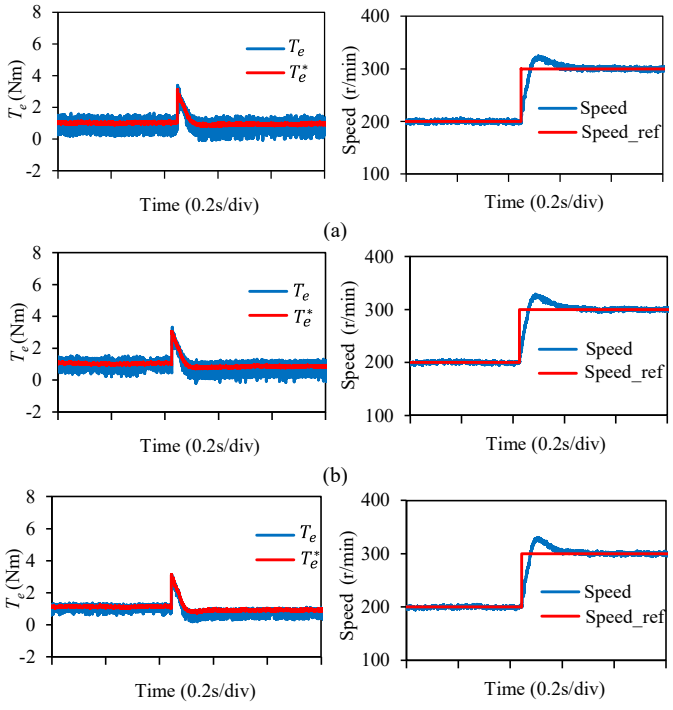

Fig. 19 Dynamic performance with speed changing from 200r/min to 300r/min at the torque 1.0 Nm. (a) Classical ST-DTC. (b) Synthetic vector ST-DTC [21]. (c) Proposed ST-DTC.

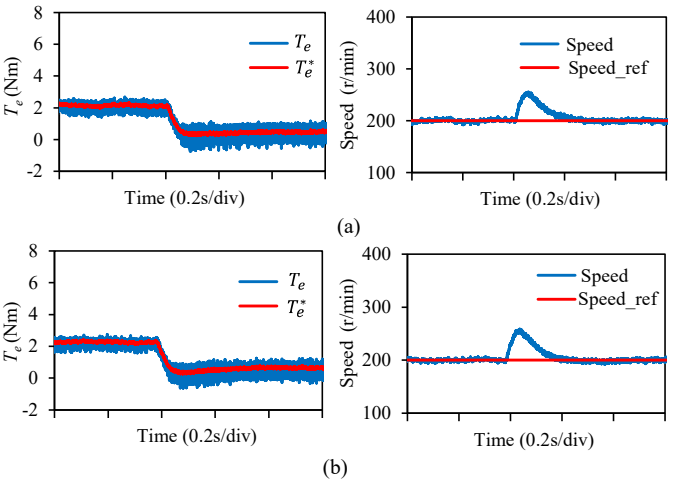

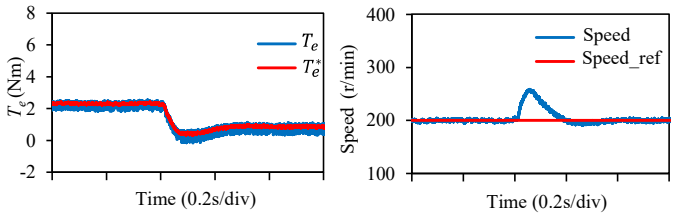

(c)

Fig. 20 Dynamic performance with torque changing from 2Nm to 0.5Nm at the speed of 200 r/min. (a) Classical ST-DTC. (b) Synthetic vector ST-DTC [21]. (c) Proposed ST-DTC.

VII. Simulation Results with Large Back-EMF Distortion

In order to further demonstrate the benefits of the proposed ST-DTC apparently, the ideal simulation model with the parameters from Table V is developed. However, this model includes larger (~ three times) 5th harmonic amplitude, reaching 1.17V in Phase A for example, in the back-emf with respect to the experimentally measured results, as shown in Fig. 14(a), (b) and Fig. 21(a), (b). Meanwhile, there are no inverter nonlinearities in the simulation. The same PIR controller parameters as in the experimental prototype are used. From Fig. 22(a) and (b) it can be seen that the 5th order harmonic in the stator current of 0.88A (caused mainly by the 5th harmonic in the back-emf) is more apparent when the synthetic vector ST-DTC is implemented. After applying the proposed ST-DTC, the harmonic currents are highly suppressed to 0.03A. Fig. 22(c) and (d) present the waveforms of i_x and i_y and their harmonic spectrums. The 5th order harmonic currents in i_x and i_y are suppressed in proposed ST-DTC. Fig. 22(e) shows the voltages in x-y subspace of synthetic vector ST-DTC and proposed ST-DTC.

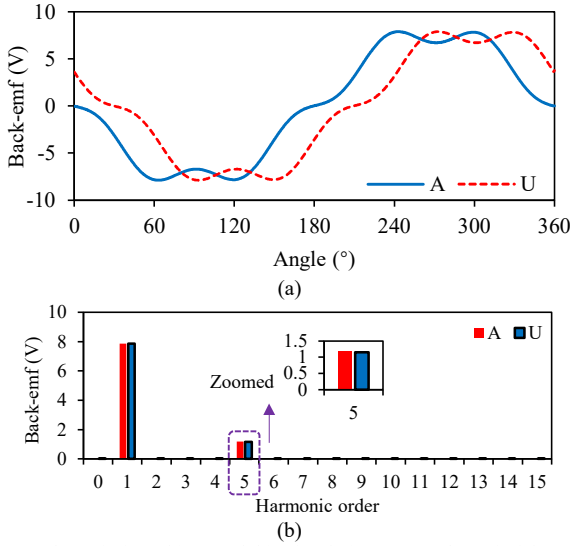

(a)

(b)

Fig. 21 Back-emf of machine model in simulation. (a) Back-emf of the machine model. (b) Back-emf spectrum analysis.

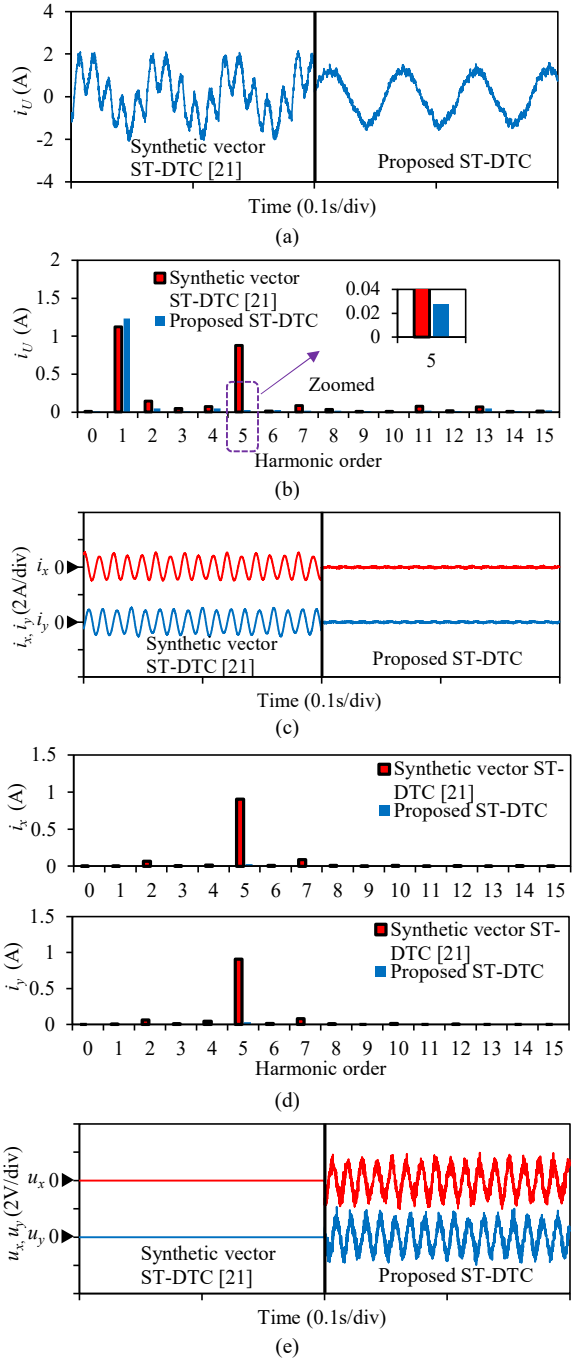

(a)

(b)

(c)

(d)

(e)

Fig. 22 Simulation comparison of synthetic vector ST-DTC and proposed ST-DTC with large EMF distortion. (a) Phase U current. (b) Spectrum analysis of Phase U current. (c) Currents in x-y subspace. (d) Spectrum analysis of currents in x-y subspace. (e) Voltages in x-y subspace.

VIII. Conclusion

The new ST-DTC for dual 3-ph PMSMs is developed and analyzed in this paper. It preserves the simple and robust structure of the classical ST-DTC, with the inclusion of the x-y current harmonics closed-control loops and modified switching table. It can compensate for stator current harmonics caused by various sources, such as dead-time, back-emf, and stator

winding asymmetries. This is in addition to the suppression of current harmonics excited in the x-y subspace.

In the proposed ST-DTC one group of three voltage vectors is employed in one sampling period. Vector groups are decided in the α-β subspace based on torque and flux requirements while the dwell times of selected voltage vectors are determined in the x-y subspace based on the outputs of the x-y current loops. Since the aim of the added x-y current control loops in this work is to suppress stator current harmonics, the x-y current references are set to zero. However, the proposed ST-DTC can be also employed to inject current harmonics for specific optimization purposes.

Though the proposed ST-DTC has a relatively low DC link voltage utilization rate, the other identified set of three-voltage-vector groups formed by three longest voltage vectors in α-β subspace can be implemented for applications requiring a large DC link voltage utilization rate and a small linear range in x-y subspace. Alternatively, a combination of the proposed ST-DTC and the synthetic vector ST-DTC switched by the multi-level hysteresis torque controller can be a solution.

REFERENCES

[1] I. Takahashi and T. Noguchi, "A new quick-response and high-efficiency control strategy of an induction motor," *IEEE Trans. Ind. Appl.*, vol. 22, no. 5, pp. 820–827, Sep. 1986.

[2] X. T. Garcia, B. Zigmund, A. Terlizzi, Rastislav Pavlanin, and L. Salvatore, "Comparison between FOC and DTC strategies for permanent magnet synchronous motors," *Adv. Electr. Electron. Eng*., vol. 5, no. 1, pp. 76-81, Jun. 2011.

[3] F. Niu, B. Wang, A. S. Babel, K. Li, and E. G. Strangas, "Comparative evaluation of direct torque control strategies for permanent magnet synchronous machines," *IEEE Trans. Power Electron.*, vol. 31, no. 2, pp. 1408–1424, Feb. 2016.

[4] T. Noguchi, M. Yamamoto, S. Kondo, and I. Takahashi, "High frequency switching operation of PWM inverter for direct torque control of induction motor," in *Conf. Rec. IEEE-IAS Annu. Meet.*, New Orleans, LA, USA, 1997, pp. 775–780.

[5] K. B. Lee, J. H. Song, I. Choy, and J. Y. Yoo, "Torque ripple reduction in DTC of induction motor driven by three-level inverter with low switching frequency," *IEEE Trans. Power Electron.*, vol. 17, no. 2, pp. 255–263, Mar. 2002.

[6] K. Gulez, A. A. Adam, and H. Pastaci, "A novel direct torque control algorithm for IPMSM with minimum harmonics and torque ripples," *IEEE/ASME Trans. Mechatron.*, vol. 12, no. 2, pp. 223–227, Apr. 2007.

[7] G. H. B. Foo and X. Zhang, "Constant switching frequency based direct torque control of interior permanent magnet synchronous motors with reduced ripples and fast torque dynamics," *IEEE Trans Power Electron.*, vol. 31, no. 9, pp. 6485–6493, Sep. 2016.

[8] D. Telford, M. W. Dunnigan, and B. W. Williams, "A novel torque-ripple reduction strategy for direct torque control of induction motor," *IEEE IEEE Trans. Ind. Electron.*, vol. 48, no. 4, pp. 867–870, Aug. 2001.

[9] E. Levi, "Multiphase electric machines for variable-speed applications," *IEEE Trans. Ind. Electron.*, vol. 55, no. 5, pp. 1893–1909, May 2008.

[10] E. Levi, R. Bojoi, F. Profumo, H. Toliyat, and S.Williamson, "Multiphase induction motor drives—A technology status review," *IET Elect. Power Appl.*, vol. 1, no. 4, pp. 489–516, Jul. 2007.

[11] E. Levi, "Advances in converter control and innovative exploitation of additional degrees of freedom for multiphase machines," *IEEE Trans. Ind. Electron.*, vol. 63, no. 1, pp. 433–448, Jan. 2016.

[12] H. Xu, H.A. Toliyat, and L.J. Petersen, "Five-phase induction motor drives with DSP-based control system", *IEEE Trans Power Electron.*, vol. 17, no. 4, pp. 524-533, Jul. 2002.

[13] L. Gao, J. E. Fletcher, and L. Zheng, "Low-speed control improvements for a two-level five-phase converter-fed induction machine using classic direct torque control," *IEEE Trans. Ind. Electron.*, vol. 58, no. 7, pp. 2744–2754, Jul. 2011.

[14] Y. N. Tatte and M. V. Aware, "Direct torque control of five-phase induction motor with common-mode voltage and current harmonics reduction," *IEEE Trans. Power Electron.*, vol. 32, no. 11, pp. 8644–8654, Nov. 2017.

[15] A. Taheri, A. Rahmati, and S. Kaboli, "Efficiency improvement in DTC of six-phase induction machine by adaptive gradient descent of flux," *IEEE Trans. Power Electron.*, vol. 27, no. 3, pp. 1552–1562, Mar. 2012.

[16] J. K. Pandit, M. V. Aware, R. V. Nemade, and E. Levi, "Direct torque control scheme for a six-phase induction motor with reduced torque ripple," *IEEE Trans. Power Electron.*, vol. 32, no. 9, pp. 7118–7129, Sep. 2017.

[17] J. K. Pandit, M. V. Aware, R. Nemade, and Y. Tatte, "Simplified implementation of synthetic vectors for DTC of asymmetric six-phase induction motor drives," *IEEE Trans. Ind. Appl.*, vol. 54, no. 3, pp. 2306–2318, May 2018.

[18] R. Bojoi, F. Farina, G. Griva, F. Profumo, and A. Tenconi, "Direct torque control for dual three-phase induction motor drives," *IEEE Trans. Ind. Appl.*, vol. 41, no. 6, pp. 1627–1636, Nov. 2005.

[19] Y. Zhao and T. Lipo, "Space vector PWM control of dual three-phase induction machine using vector space decomposition," *IEEE Trans. Ind. Appl.*, vol. 31, no. 5, pp. 1100–1109, Sep. 1995.

[20] K. D. Hoang, Y. Ren, Z. Q. Zhu, and M. Foster, "Modified switching-table strategy for reduction of current harmonics in direct torque controlled dual three-phase permanent magnet synchronous machine drives," *IET Elect. Power Appl.*, vol. 9, no. 1, pp. 10–19, Jan. 2015.

[21] Y. Ren and Z. Q. Zhu, "Enhancement of steady-state performance in direct torque controlled dual-three phase permanent magnet synchronous machine drives with modified switching table," *IEEE Trans. Ind. Electron*., vol. 62, no. 6, pp. 3338-3350, Jun. 2015.

[22] Y. Ren and Z. Q. Zhu, "Reduction of both harmonic current and torque ripple for dual three-phase permanent-magnet synchronous machine using modified switching-table-based direct torque control," *IEEE Trans. Ind. Electron.*, vol. 62, no. 11, pp. 6671–6683, Nov. 2015.

[23] B. Yu, W. Song, J. Li, B. Li, and M. S. R. Saeed, "Improved finite control set model predictive current control for Five-Phase VSIs," *IEEE Trans. Power Electron.*, to be published. DOI: 10.1109/TPEL.2020.3034756.

[24] H. Vu and H. Lee, "Model predictive current control scheme for seven-phase voltage source inverter with reduced common-mode voltage and current harmonics," *IEEE Trans. J. Emerg. Sel. Topics Power Electron.*, to be published. DOI: 10.1109/JESTPE.2020.3009392.

[25] A. H. Abosh, Z. Q. Zhu, and Y. Ren, "Reduction of torque and flux ripples in space vector modulation-based direct torque control of asymmetric permanent magnet synchronous machine," *IEEE Trans. Power Electron*., vol. 32, no. 4, pp. 2976-2986, Apr. 2017.

[26] H. S. Che, E. Levi, M. Jones, W. P. Hew, and N. A. Rahim, "Current control methods for an asymmetrical six-phase induction motor drive," *IEEE Trans. Power Electron*., vol. 29, no. 1, pp. 407–417, Jan. 2014.

[27] G. Liu, B. Chen, K. Wang, and X. Song, "Selective current harmonic suppression for high-speed PMSM based on high-precision harmonic detection method," *IEEE Trans. Ind. Informat.*, vol. 15, no. 6, pp. 3457-3468, Jun. 2019.

[28] J. Hwang and H. Wei, "The current harmonics elimination control strategy for six-leg three-phase permanent magnet synchronous motor drives," *IEEE Tran. Power Electron.*, vol. 29, no. 6, pp. 3032-3040, Jun. 2014.

[29] Q. An, X. Liu, Q. An, S. Li, and K. Bi, "Current harmonics suppression of permanent magnet synchronous motor based on repetitive control," in *Proc. ITEC Asia-Pacific*, Bangkok, Thailand, 2018, pp. 1-7.

[30] D. Li, Y. Iwaji, Y. Notohara, and K. Kishita, "Harmonic current cancellation method for PMSM drive system using resonant controllers," in *Proc. IPEC-ECCE Asia*, Niigata, Japan, 2018, pp. 1301-1307.

[31] M. Jones, D. Dujic, E. Levi, and S. N. Vukosavic, "Dead-time effects in voltage source inverter fed multi-phase AC motor drives and their mitigation," in *Proc. 13th Eur. Conf. Power Electron. Appl*., Barcelona, Spain, 2009, pp. 1–10.

[32] M. Jones, S. N. Vukosavic, D. Dujic, and E. Levi, "A synchronous current control scheme for multiphase induction motor drives," *IEEE Trans. Energy Convers.*, vol. 24, no. 4, pp. 860–868, Dec. 2009.

[33] Y. Zhu, W. Gu, K. Lu, Z. Wu, J. Guan, and L. Chen, "Current harmonic elimination method for asymmetric dual three-phase permanent magnet

synchronous motor," *IET Electr. Power Appl.*, vol. 14, no. 10, pp. 1795-1806, Sep. 2020.

[34] Y. Hu, Z. Zhu, and K. Liu, "Current control for dual three-phase permanent magnet synchronous motors accounting for current unbalance and harmonics," *IEEE J. Emerg. Sel. Topics Power Electron.*, vol. 2, no. 2, pp. 272-284, Jun. 2014.

[35] J. Hu, H. Nian, H. Xu, and Y. He, "Dynamic modeling and improved control of DFIG under distorted grid voltage conditions," *IEEE Trans. Energy Convers.*, vol. 26, no. 1, pp. 163–175, Mar. 2011.

[36] H. Chen and H. Zhao, "Review on pulse-width modulation strategies for common-mode voltage reduction in three-phase voltage-source inverters," *IET Power Electron*., vol. 9, no. 14, pp. 2611-2620, Nov. 2016.

[37] Y. S. Lai, "Investigations into the effects of PWM techniques on common mode voltage for inverter-controlled induction motor drives," in *Proc. IEEE PES Winter Meet.*, New York, NY, USA, 1999, pp. 35–40.

[38] A. M. Hava and E. Un, "Performance analysis and comparison of reduced common mode voltage PWM and standard PWM techniques for three-phase voltage source inverters," in *Proc. IEEE APEC*, Dallas, TX, USA, 2006, pp. 303–309.